RSC Advances

RSC Publishing

PAPER

View Article Online
View Journal | View Issue

Redox behaviour, electrochromic properties and photoluminescence of potassium lanthano phosphomolybdate sandwich-type compounds†

Cite this: *RSC Advances*, 2013, **3**, 16697

Diana M. Fernandes,[a] Luís Cunha-Silva,[a] Rute A. S. Ferreira,[b] Salete S. Balula,[a] Luis D. Carlos,[b] Baltazar de Castro[a] and Cristina Freire*[a]

Received 9th April 2013,
Accepted 9th July 2013

DOI: 10.1039/c3ra41697f

www.rsc.org/advances

Sandwich type phosphomolybdates with general formula $K_n[Ln^{III}(PMo_{11}O_{39})_2]$, where Ln^{III} = Sm, Eu, Gd, Tb and Dy, were prepared and characterized by several techniques. The crystal structure of $Sm(PMo_{11})_2$ and $Gd(PMo_{11})_2$ were studied and showed that they crystallise in a $P2_1/c$ space group. All $Ln(PMo_{11})_2$ revealed four Mo based electrochemical reduction processes with very similar $E_{1/2}$ values ($\approx$0.5, $\approx$0.3, $\approx$0.02 and ≈ -0.1 V) for all the Ln^{III} atoms. The two more positive reduction processes correspond to pH independent one electron reduction processes, whereas the two more negative processes correspond to pH dependent two electron reduction processes. Electrolysis at two different potentials, 0.1 V related to the two one electron reduction processes and −0.3 V related to the two more negative two electron reduction processes, confirmed the electrochromic properties of the $Ln(PMo_{11})_2$ species: their original yellow coloured solutions turned blue, corresponding to the appearance of four new electronic bands in the near UV Vis near IR region. These electronic bands were tentatively assigned based on their molar absorption coefficients (ε) and absorbance (Abs) variation as a function of electrolysis time: bands A ($\lambda_{max} \approx$ 855 870 nm) and B ($\lambda_{max} \approx$ 670 695 nm) were assigned to $Mo^{V} \rightarrow Mo^{VI}$ intervalence charge transfer transitions, band C ($\lambda_{max} \approx$ 525 nm) to d d transition due to d^1 configuration of the reduced addenda atom (Mo^{V}) and band D ($\lambda \approx$ 310 315 nm) to an $O \rightarrow Mo^{V}$ charge transfer transition (CTT). The emission features of the $Eu(PMo_{11})_2$ and $Tb(PMo_{11})_2$ samples reveal broad emission in the UV/vis spectral region resulting from d d transition transitions. The $Eu(PMo_{11})_2$ also display the typical Eu^{3+} $^5D_0 \rightarrow {}^7F_{0-4}$ transitions, when excited through the $O \rightarrow Eu^{III}$ and $O \rightarrow Mo^{VI}$ CCTs.

1. Introduction

Polyoxometalates (POMs) are a well-known class of structurally well-defined metal oxide clusters with rich framework topologies, compositions and relevant properties.[1–6] One of the most promising properties of these metal oxide clusters is the rich redox chemistry as they can accept electrons to become mixed-valence colored species namely ''heteropoly blue''. This outstanding property makes them good candidates for photochromic and electrochromic materials.[7] However, in comparison with the large number of studies on other electrochromic materials, such as transition metal oxides.[8,9] Prussian blue,[9,10] viologens[9,11] and conducting polymers,[12] the study of electrochromism based on POMs has been not often reported.

Recently, the lanthanide heteropolyoxometalate complexes have attracted renewed interest due to the ability of Ln^{III} cations to coordinate polyoxometalate anions forming extended structures in the solid state.[13–15] One of the simplest structural types, first reported by Peacock and Weakley, are the LnL_2 complexes (L = $[SiW_{11}O_{39}]^8$, *etc.*), in which two lacunary Keggin anions encapsulate an 8-coordinate Ln^{III} cation by coordination through the 4 surface unsaturated oxygen at the lacunary defect site.[16] The lanthanide complexes, $[Ln^{III}(PW_{11}O_{39})_2]$[11] are known to be stable and have been prepared and characterized, although not fully structurally characterized.[17–19] Some related heteropolyoxomolybdate complexes have been prepared and crystallographically characterized, including $K_7H_6[Nd(GeMo_{11}O_{39})_2]\cdot 27H_2O$[20] and $K_{11}H_2[Dy(SiMo_{11}O_{39})_2]\cdot 29H_2O$.[21]

Recently, the structural characterization of a series of phosphomolybdate complexes of general formula $(NH_4)_{11}[Ln^{III}(PMo_{11}O_{39})_2]\cdot 16H_2O$ (where Ln^{III} = La, Sm, Eu, Gd, Tb, Dy, Ho, Er, Tm, Yb, Lu, Ce and Nd)[22,23] were prepared and characterized. However, in the literature few reports can be found concerning the redox and electrochromic properties

[a]*REQUIMTE, Departamento de Química e Bioquímica, Faculdade de Ciências, Universidade do Porto, 4169 007 Porto, Portugal. E mail: acfreire@fc.up.pt; Fax: +351 22 0402 695; Tel: +351 22 04020590*

[b]*Department of Physics and CICECO, University of Aveiro, 3810 193 Aveiro, Portugal*

† Electronic supplementary information (ESI) available. See DOI: 10.1039/c3ra41697f

of this type of compounds; these include the $Dy(SiMo_{11})_2$[24] and the related $Nd(SiMo_7W_4O_{39})_2$ mixed heteropolyanion.[25]

In the present work, the preparation of potassium salts of general formulae $K_n[Ln^{III}(PMo_{11}O_{39})_2]$, where Ln^{III} = Sm, Eu, Gd, Tb and Dy, is described; throughout investigations of these systems we focused, in addition to the structural and electronic characterization, on the redox and electrochromic properties of the compounds in solution and the photoluminescent in solid state with the ultimate goal to use these compounds as tectons in the fabrication of functional nanostructured films.

2. Experimental

2.1. Materials

Phosphomolybdic acid hydrate, terbium(III) chloride hexahydrate (99.9%), europium(III) chloride hexahydrate (99.9%), samarium(III) chloride hexahydrate (99.9%), dysprosium(III) chloride hexahydrate (99.9%), gadolinium(III) chloride hexahydrate (99.9%), potassium carbonate (>99.0%) all from Aldrich, sulphuric acid (95–97%) from VWR, sodium sulphate (99.5%) from Prolabo, ethanol absolute from Fisher Chemical and acetonitrile from Romil, were used as received. Electrolyte solutions for voltammetry were prepared using ultra-pure water (resistivity 18.2 MΩ cm at 25 °C, Millipore). Buffer solutions within the pH range 2.5–4.0 were prepared by mixing appropriate amounts of a 0.2 mol dm^{-3} H_2SO_4 solution with a 0.5 mol dm^{-3} Na_2SO_4 solution.

2.2. Synthesis of the compounds

The compounds with general formula $K_{11}[Ln^{III}(PMo_{11}O_{39})_2]\cdot xH_2O$ (Ln^{III} = Sm, Eu, Gd, Tb and Dy) were prepared by a procedure adapted from the literature:[22,23] the compound $H_3PMo_{12}O_{40}$ (0.002 mol) was dissolved in H_2O (0.02 dm^3) with stirring and the pH was adjusted up to 4.3 by the addition of K_2CO_3 to yield $[PMo_{11}O_{39}]^{7-}$ (denoted as PMo_{11}) as the dominant phosphomolybdate species.[26,27] Then the lanthanide salt, $Ln^{III}Cl_3\cdot{}_6H_2O$ with Ln^{III} = Sm, Eu, Gd, Tb and Dy, was added to the previous solution in a 2 : 1 PMo_{11} : Ln^{III} ratio; the pH of the solution was re-adjusted to 4.3 by the addition of more K_2CO_3. Finally, KCl (0.0549 mol) was added to the solution which was left stirring for 1h; in the case of Eu^{III} and Tb^{III} based compounds, EtOH was added to induce the precipitation of the bulk solids. In the end all the solids were dried under vacuum for overnight. The prepared compounds are denoted as $Ln(PMo_{11})_2$, in which Ln is Sm, Eu, Gd, Tb and Dy.

Crystals suitable for X-ray diffraction were prepared by storing the final solutions for one week at 5 °C; for Sm^{III}, Gd^{III} and Dy^{III}, a small volume of CH_3CN was used to induce crystallisation.

2.3. Physical measurements

The Fourier transform infrared (FTIR) spectra of $Ln(PMo_{11})_2$ were performed in a Jasco FT/IR-460 Plus spectrophotometer in the range 400–4000 cm^{-1}, using a resolution of 4 cm^{-1} and 32 scans; the spectra were obtained in KBr pellets (Merck, spectroscopic grade). The ^{31}P nuclear magnetic resonance (^{31}P NMR) spectra were obtained in D_2O in a Bruker Anance III 400 and referenced against H_3PO_4 (85%).

Thermogravimetric analyses (TGA) were carried out at LSRE/LCM, Departamento de Engenharia Química, Faculdade de Engenharia da Universidade do Porto, Portugal, on a Netzsch STA 409 PC/PG thermobalance, from 50 to 800 °C, with a heating rate of 5 °C min^{-1} under air flow (50 mL min^{-1}).

The electronic spectra of $Ln(PMo_{11})_2$ and the corresponding electro-reduced species were obtained in 0.1 mol dm^{-3} H_2SO_4/Na_2SO_4 buffer solution (pH 3.0) and were recorded on a Varian Cary 50 Bio spectrophotometer in the range 190–1100 nm, at room temperature, using quartz cells with 1 cm optical path. A set of 12 solutions of each $Ln(PMo_{11})_2$ (1.0×10^{-7} to 2.0×10^{-5} mol dm^{-3}) was used to determine the molar absorption coefficients of the observed electronic bands. In the case of the reduced species the molar absorption coefficients of the new bands were obtained considering the absorbance value after 6h of electrolysis and a solution concentration of 1.0×10^{-4} mol dm^{-3}.

The photoluminescence spectra of the solid compounds were recorded at 12 K and at room temperature with a modular double grating excitation spectrofluorimeter with a TRIAX 320 emission monochromator (Fluorolog-3, Horiba Scientific) coupled to a R928 Hamamatsu photomultiplier. Emission spectra (acquired using the front face mode) were corrected for the spectral response of the monochromators and the detector, using typical correction spectrum provided by the manufacturer, and the excitation spectra were corrected for the spectral distribution of the lamp intensity, using a photodiode reference detector. The emission time resolved spectra and emission decay curves were acquired at 12 K with the same instrumentation, using a pulsed Xe–Hg lamp (6 μs pulse at half width and 20–30 μs tail). The temperature was controlled with a precision of 0.1 °C, using a He closed-cycle cryostat (APD Cryogenics-HC2) coupled to an auto-tuning temperature controller (Lakeshore 330).

The electrochemical measurements were carried out using an Autolab PGSTAT 30 potentiostat/galvanostat (EcoChimie B.V.) controlled by GPES software. Cyclic voltammetric measurements were performed at room temperature using a conventional three-electrode compartment cell with a glassy carbon electrode, GCE, (3 mm diameter, BAS, MF-2012) as the working electrode, and the auxiliary and reference electrodes were platinum wire (7.5 cm, BAS, MW-1032) and Ag/AgCl (sat. KCl) (BAS, MF-2052), respectively. The cell was enclosed in a grounded Faraday cage and kept under flowing argon during experiments. Prior to use, the GCE was polished with aluminium oxide of particle size 0.3 μm (Buehler-Masterprep) on a microcloth polishing pad (BAS Bioanalytical Systems Inc.), and then was rinsed with ultra-pure water and finally sonicated for 5 min in an ultrasonic bath (FUNGILAB). The electrolysis was performed at constant potential, 0.1 and −0.3 V, at room temperature, for 6 h, using a three-electrode compartment cell with a Reticulated Vitreous Carbon Electrode, RVCE, (50 mm high, 40 mm diameter, and 5 mm thick, RVC surface area is 10.5 cm^2 cm^{-3}, MF-2077) as the working electrode, and the auxiliary and reference electrodes were platinum wire (7.5 cm, BAS, MW-1032) and Ag/AgCl (sat.

KCl) (BAS, MF-2052), respectively. In all electrochemical experiments an argon atmosphere was used.

A combined glass electrode (Crison) connected to a pH meter Basic 20$^+$ (Crison) was used for the pH measurements.

2.4. Single-crystal X-ray diffraction

Crystalline materials suitable for single-crystal X-ray diffraction analysis of $K_{11}[Ln(PMo_{11}O_{39})_2]\cdot xH_2O$ [$Ln(PMo_{11})_2$; Ln^{3+} = Sm^{3+}, Eu^{3+}, Gd^{3+}, Tb^{3+} and Dy^{3+}] were harvested and mounted in a Hampton CryoLoops using adequate viscous oil.[28] Diffraction data were collected at 150 K on a Bruker X8 Kappa APEX II charge-coupled device (CCD) area-detector diffractometer (Mo-Kα graphite-monochromated radiation) controlled by the APEX2 software,[29] and equipped with an Oxford Cryosystems Series 700 cryostream monitored remotely by the Cryopad interface.[30] Full acquisitions were performed for $Sm(PMo_{11})_2$ and $Gd(PMo_{11})_2$, while the remaining compounds were only indexed. Images were processed with SAINT+ software,[31] and the absorption corrections were performed by the multi-scan method implemented in SADABS.[32] The structures were solved by direct methods implemented in SHELXS-97,[33,34] leading to the identification of most of the heaviest elements, namely Ln and Mo atoms, while the remaining atoms were positioned through successive full-matrix least squares refinement cycles on F^2 using SHELXL-97.[33,35] All atoms of the lanthano-phosphomolybdate anions and the K^+ cations were refined using anisotropic displacement parameters, while the hydration water molecules were refined with isotropic parameters. Even though the H-atoms of the crystallization water molecules could not be located from difference Fourier maps or even placed in calculated positions, were added to the molecular formula of the compounds.

Crystallographic data collection and structure refinement details are summarized in Table 1. Crystallographic information (excluding structure factors) for $Sm(PMo_{11})_2$ and $Gd(PMo_{11})_2$ structures can be obtained free of charge *via* http://www.fiz-karlsruhe.de/obtaining crystal structure data.html or from the Inorganic Crystal Structure Database (ICSD, FIZ Kalsruhe, Hermann-von-Helmholtz-Platz 1, Eggenstein-Leopoldshafen, 76344, Germany; phone: +49 7247808555, fax: +49 7247808259; e-mail: crysdata@fiz-karlsruhe.de), on quoting the depository numbers CSD 426000 and CSD 425999.

3. Results and discussion

3.1. Structural and spectroscopic characterization

The reaction of the monovacant polyoxometalate $[PMo_{11}O_{39}]^7$ with the lanthanide ions, Sm^{III}, Eu^{III}, Gd^{III}, Tb^{III} and Dy^{III}, in the presence of potassium cations lead to the formation of sandwich compounds of general formula $K_n[Ln^{III}(PMo_{11}O_{39})_2]\cdot xH_2O$.

The compounds show TGA curves with similar weight loss profile: an initial weight loss of ~2.3 to 2.7 wt% in the temperature range of 50–200 °C corresponding to the release of crystal water molecules and adsorbed water molecules and a second major weight loss observed at temperatures higher than 200 °C that is due to the thermal disruption of the heteropolyanion structure. The first weight loss permits the determination of the number of water molecules for the prepared compounds: 6 for Ln^{III} = Eu and Tb and 10 for Ln^{III} =

Table 1 Crystal and structure refinement data for $Ln(PMo_{11})_2$ (Ln^{3+} = Sm^{3+}, Eu^{3+}, Gd^{3+}, Tb^{3+} and Dy^{3+})

	$Sm(PMo_{11})_2$	$Eu(PMo_{11})_2$	$Gd(PMo_{11})_2$	$Tb(PMo_{11})_2$	$Dy(PMo_{11})_2$
Formula	$K_{11}H_{54}P_2Mo_{22}O_{105}Sm$		$K_{44}H_{248}P_8Mo_{88}O_{437}Gd_4$		
Formula weight	4487.50		18 281.87		
Crystal description	yellow needles	yellow needles	yellow needles	yellow needles	yellow needles
Crystal size (mm)	0.17 × 0.08 × 0.02	0.29 × 0.06 × 0.03	0.24 × 0.08 × 0.04	0.17 × 0.06 × 0.02	0.20 × 0.08 × 0.03
T (K)	150.0(2)	150.0(2)	150.0(2)	150.0(2)	150.0(2)
Crystal system	Monoclinic	Monoclinic	Monoclinic	Monoclinic	Monoclinic
Space group	$P2_1/c$	Bravais lattice P	$P2_1/c$	Bravais lattice P	Bravais lattice P
a (Å)	18.762(7)	18.53	18.4137(7)	18.45	18.30
b (Å)	37.725(13)	37.73	37.4667(15)	36.92	37.52
c (Å)	14.263(7)	14.15	14.0757(6)	13.96	14.06
α (°)	90	90	90	90	90
β (°)	91.44(2)	92.47	92.871(2)	92.57	92.35
γ (°)	90	90	90	90	90
Volume (Å^3)	10 092(7)	9886.8	9698.6(7)	9509.2	9653.8
Z	4		1		
$\rho_{calculated}$ (g cm ^{3})	2.953		3.130		
μ (mm ^{1})	3.813		4.052		
θ range (°)	3.54 to 25.03		3.70 to 26.37		
Index ranges	$-22 \leqslant h \leqslant 22$, $-44 \leqslant k \leqslant 44$, $-14 \leqslant l \leqslant 16$		$-23 \leqslant h \leqslant 23$, $-46 \leqslant k \leqslant 46$, $-17 \leqslant l \leqslant 12$		
Reflections collected	58 381		77 779		
Independent reflections	17 455 (R_{int} 0.1045)		19 762 (R_{int} 0.0500)		
Final R indices [$I > 2\sigma(I)$]	R_1 0.0600, wR_2 0.1427		R_1 0.0486, wR_2 0.1054		
Final R indices (all data)	R_1 0.0999, wR_2 0.1667		R_1 0.0691, wR_2 0.1166		
Largest diff. peak and hole (e Å ^{3})	2.856 and −2.803		3.154 and −1.867		

Sm, Gd and Dy. These values are smaller than those observed by crystal X-ray diffraction (see below) due to the fact that the bulk materials were dried in vacuum at the end of their preparation.

For all the compounds it was possible to isolate crystalline materials suitable for single-crystal X-ray analysis. However, it was only possible to make full data collections and structure determinations for the Sm and Gd based compounds. The crystals of the remaining materials revealed weak diffraction and problematic radiation scattering, despite several attempts have been performed with many crystals of each compound. Consequently, for the Eu, Tb and Dy based compounds it was only possible to perform the determination of the cell parameters (indexing), Table 1. These parameters are identical among all the prepared $Ln(PMo_{11})_2$, suggesting that all the compounds were isolated in the same crystalline phase and are structurally similar. The $Sm(PMo_{11})_2$ and $Gd(PMo_{11})_2$ materials are isostructural, crystallizing in the monoclinic system with the respective structures solved in the space $P2_1/c$ group, thus the structural details will be only discussed for the Gd based compound.

The asymmetric unit of $Gd(PMo_{11})_2$ crystal structure reveal one $[Gd(PMo_{11}O_{39})_2]^{11}$ anion, and 11 K^+ cations distributed over 14 positions and several crystallization water molecules. The gadolinium–phosphomolybdate anion shows one Gd^{3+} centre encapsulated by two monolacunary Keggin units $[PMo_{11}O_{39}]^7$ (Fig. 1). As reported for identical lanthano-phosphomolybate anions in ammonium salt compounds, $(NH_4)_{11}[Ln(PMo_{11}O_{39})_2]\cdot xH_2O$, the gadolinium ion is connected by eight lacunary O-atoms belonging at two Keggin fragments originating an eight coordinated centre, (GdO_8).[22,23] Actually, in coordination centres of type LnO_8 there are the possibility of three distinct polyhedral geometries: dodecahedral (crystallographic pointing group D_{2h}), square anti-prism (D_{4h}) and bicapped trigonal prism (C_{2v}). The coordination environment of GdO_8 resembles more a square-antiprismatic geometry, due to the relative rotation of the two $[PMo_{11}O_{39}]^7$ moieties. In fact, the relative orientation between the two idealized squares defined by the coordination O-atoms is *ca.* 40°. The angle between the normal vectors of the oxygen-based square planes is 3.1(2)° and the distance between the two square planes (interplanar distance) is 2.537(6)5 Å, while the closer and longer O···O distances within the oxygen-based square planes range in 2.758(8)–2.9286(8) Å and 4.024(8)–4.066(8) Å, respectively. The main structural characteristics of the $[Gd(PMo_{11}O_{39})_2]^{11}$ anion are comparable to that already reported for related compounds.[22,23] The inspection of the Ln–O bond distances in the $Sm(PMo_{11})_2$ and $Gd(PMo_{11})_2$ structures confirms the expected trend of bond length contraction across the lanthanide series: averages Sm–O and Gd–O bond distances are 2.427(9) and 2.389(6) Å, respectively, Table 2. This contraction is a consequence of the stronger interaction between the lanthanides and the oxygen atoms with the ionic radius decreasing the lanthanides.

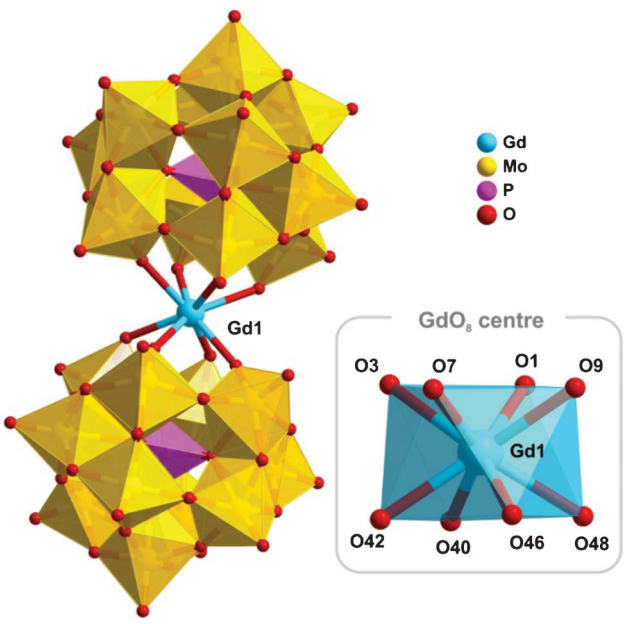

Fig. 1 The sandwich type lanthano phosphomolybdate anion, $Gd(PMo_{11}O_{39})_2^{11-}$ (left), and the {GdO_8}coordination centre displaying a square antiprismatic geometry (right), drawn in polyhedral and ball and stick mixed model.

Table 2 Selected bond lengths (in Å) for the Sm^{3+} and Gd^{3+} coordination environments found in $Sm(PMo_{11})_2$ and $Gd(PMo_{11})_2$

Sm1 O1	2.463(9)	Gd1 O1	2.384(6)
Sm1 O3	2.401(9)	Gd1 O3	2.375(6)
Sm1 O7	2.418(9)	Gd1 O7	2.399(6)
Sm1 O9	2.423(8)	Gd1 O9	2.397(6)
Sm1 O40	2.445(9)	Gd1 O40	2.376(6)
Sm1 O42	2.434(9)	Gd1 O42	2.384(6)
Sm1 O46	2.415(9)	Gd1 O46	2.394(6)
Sm1 O48	2.420(9)	Gd1 O48	2.400(6)

In the extended crystal structure, the sandwich type gadolinium phosphomolybdate anions $[Gd(PMo_{11}O_{39})_2]^{13}$ are surrounded by charge balancing K^+ cations and numerous hydration water molecules, being involved in an extensive network of ionic and intermolecular (hydrogen bonds) interactions.

The infrared spectra of the lanthano polyoxomolybdates presented in Fig. S1 (A and B), ESI,† show in the region 1150–700 cm^{-1} the typical vibration bands of the polyoxomolybdates. They show two bands in the interval 1086–1033 cm^{-1}, assigned to the splitting of the P–O stretching vibration band due to the decrease in symmetry of the lacunary species in comparison with the parent Keggin anion, $[PMo_{12}O_{40}]^3$ that has T_d symmetry and hence only shows one vibration band: the removal of a Mo–O unit from the parent structure leads to an effective local C_{3v} symmetry of the PO_4 unit in the lacunary anion. Moreover, it is also observed the characteristic Mo–O_d vibration band at 934 cm^{-1} for $Gd(PMo_{11})_2$, 935 cm^{-1} for $Eu(PMo_{11})_2$, $Dy(PMo_{11})_2$ and $Sm(PMo_{11})_2$ and 936 cm^{-1} for $Tb(PMo_{11})_2$ and the bands within 876–760 cm^{-1} that are assigned to Mo–O–Mo (corner shared) and Mo–O–Mo (edge shared) stretching modes.[22,23,27] Additionally, there is a broad band centered at approximately 3500 cm^{-1} and an intense band at 1600 cm^{-1} assigned, respectively, to the stretching

and bending vibrations of the crystallization water molecules present in the lanthano polyoxomolybdates structures.

The ^{31}P NMR solution spectra of all polyoxometalates revealed one main band attributed to the presence of two equivalents phosphorus atoms in the $[Ln^{III}(PMo_{11})_2]^{11}$ anions (Fig. S2 in ESI†). For Sm^{III} and Eu^{III} based polyoxometalates very sharp bands were observed with chemical shifts of 4.06 and 10.54 ppm, respectively, but for Gd^{III}, Tb^{III} and Dy^{III} based species, the bands shifted to δ = 18.49, 155.2 and 72.17 ppm, respectively, with an increase in bandwidth. The observed band shift and broadening is due the paramagnetism associated with coordinated lanthanide cations with incomplete f^n configurations; the chemical shifts are in good agreement with previously published work for analogous compounds.[19,23]

The electronic spectra of all compounds are very similar and present two intense bands in the region 300–200 nm assigned to transitions involving electronic states from the oxide cluster, Table 4: the electronic band at $\lambda_{max} \approx 265$ nm (ε values in the range $3.0 \times 10^4 - 4.8 \times 10^4$ cm ^{1} mol ^{1} dm^3) is characteristic of Keggin structure and is attributed to a ligand-to-metal-charge transfer transition (LMCT) from the bridging oxygen atoms O_b and O_c to Mo^{VI} atoms and the band at $\lambda_{max} \approx 215$ nm (ε values in the range $7.9 \times 10^4 - 14.0 \times 10^4$ cm ^{1} mol ^{1} dm^3) is attributed to the LMCT transition from the terminal oxygen atoms to the Mo atoms ($O_t \rightarrow Mo^{VI}$).[17,36] In some cases, this latter band exhibits a shoulder at $\lambda_{max} \approx 236$ nm that can be tentatively assigned to $O \rightarrow Ln^{III}$ LMCT transition. The electronic spectra of the $[Ln^{III}(PMo_{11})_2]^{11}$ were also obtained using more concentrated solutions in order to visualize the f–f bands associated with the lanthanide ions, but only very low intense bands were observed (spectra not shown).

3.4. Redox behaviour and electrochromic properties

The electrostability of the heteropolyanions is strongly dependent on pH, and in general, their reduction processes are coupled to protonation; therefore, the pH of electrolyte solution has a great effect on their electrochemical behaviour. In this context, the electrochemical studies of the potassium $Ln(PMo_{11})_2$ salts were carried out in a systematic way in aqueous buffer solutions (H_2SO_4/Na_2SO_4) in the pH range of 2.5–4.0.

In the potential range +0.70 to 0.30 V, all the compounds show very similar electrochemical behaviour, revealing four Mo-based electrochemical processes;[24] Fig. 2(A) depicts the cyclic voltammograms of $Sm(PMo_{11})_2$ (5×10^{-4} mol dm ^{3}) in H_2SO_4/Na_2SO_4 buffer solution (pH 3.0) at different scan rates, as an example of the electrochemical behaviour of potassium $Ln(PMo_{11})_2$ salts; in Fig. S3, ESI,† are depicted the cyclic voltammograms for the other potassium $Ln(PMo_{11})_2$ salts. Table 3 summarizes the voltammetric data for all the compounds.

The E_{pc}, E_{pa} values for the heteropolyanions do not differ much from each other which indicates that the presence of the different Ln^{III} ions have no effect on the Mo based redox processes. Peak-to-peak separations (ΔE_p) of first and second redox couples are between 0.051–0.062 V, which are close to the value of one-electron electrochemical process (0.060 V).

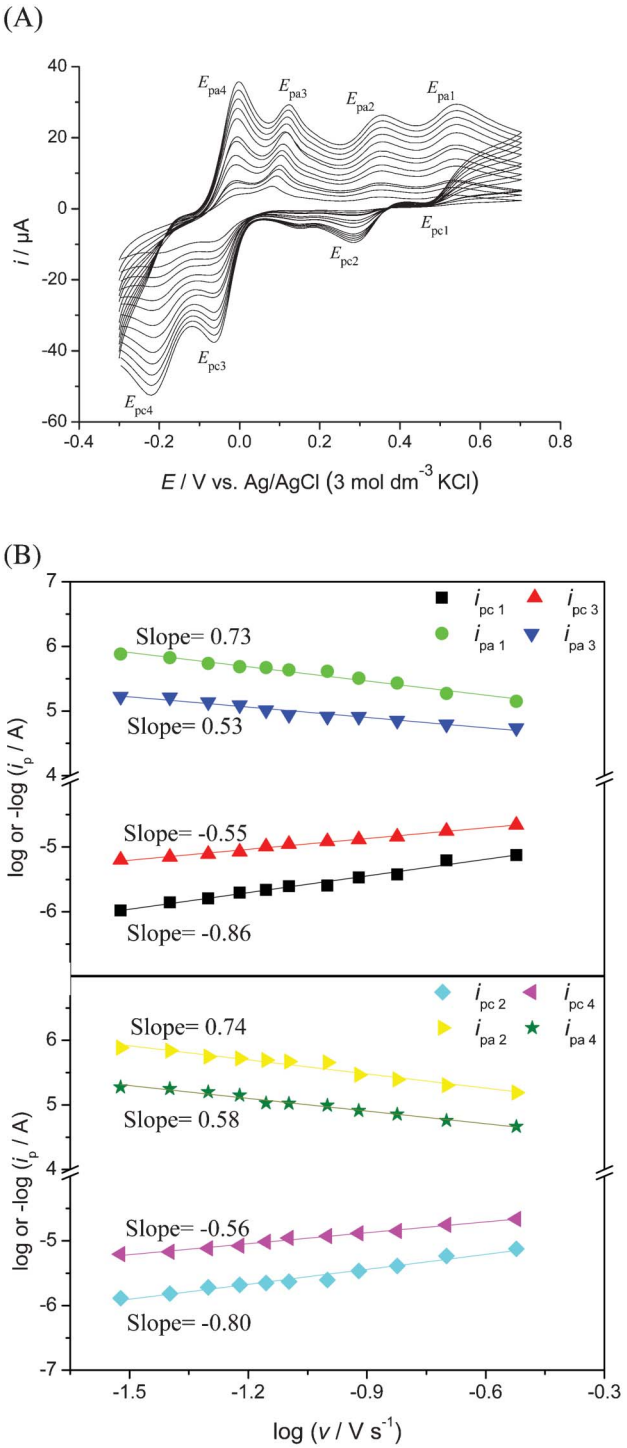

Fig. 2 A) Cyclic voltammograms of K^+ salt of $Sm(PMo_{11})_2$ (5×10^{-4} mol dm^{-3}) in pH 3.0 H_2SO_4/Na_2SO_4 buffer solution at scan rates of 0.02, 0.04, 0.06, 0.08, 0.1, 0.15, 0.2, 0.25, 0.3, 0.35, 0.4, 0.45 and 0.5 V s^{-1}. B) Plots of log i_{pc} and i_{pa} *vs.* log v for $Sm(PMo_{11})_2$.

The confirmation of the number of electrons (n) involved in the different electrochemical processes can be made by comparison of the cyclic voltammetric data of $[Fe(CN)_6]^{3/4}$ redox couple, in the same conditions as for $Ln(PMo_{11})_2$. The ratio between the peak currents of this redox couple with the

Table 3 Cyclic voltammetric data for the Mo processes in pH 3.0 H_2SO_4/Na_2SO_4 buffer solution at 0.1 V s^{-1} (potential values in V *vs.* Ag/AgCl (3 mol dm^{-3} KCl))

POM	Mo	E_{pc}	I_{pc} (μA)	$E_p - E_{p/2}$	E_{pa}	I_{pa} (μA)	$E_p - E_{p/2}$	$\lvert\Delta E_p\rvert$	$E_{1/2}$	I_{pa}/I_{pc}
$Sm(PMo_{11})_2$	1	0.482	−2.55	−0.053	0.533	2.44	0.051	0.051	0.509	−0.96
	2	0.296	−2.48	−0.040	0.348	2.20	0.044	0.052	0.322	−0.89
	3	−0.062	−12.21	−0.042	0.102	12.07	0.150	0.164	0.020	−0.99
	4	−0.201	−11.86	−0.177	−0.016	10.14	0.043	0.185	−0.109	−0.85
$Eu(PMo_{11})_2$	1	0.476	−2.93	−0.052	0.533	2.95	0.052	0.057	0.505	−1.00
	2	0.296	−2.89	−0.041	0.353	2.85	0.046	0.057	0.325	−0.99
	3	−0.063	−12.79	−0.047	0.102	12.79	0.155	0.165	0.020	−1.00
	4	−0.201	−12.57	−0.170	−0.011	12.27	0.043	0.190	−0.106	−0.98
$Gd(PMo_{11})_2$	1	0.478	−2.55	−0.050	0.540	2.19	0.044	0.062	0.509	−0.86
	2	0.296	−2.52	−0.053	0.358	2.30	0.044	0.062	0.327	−0.91
	3	−0.049	−12.92	−0.049	0.112	11.94	0.150	0.161	0.032	−0.92
	4	−0.180	−12.77	−0.186	0.002	11.09	0.044	0.184	−0.094	−0.87
$Tb(PMo_{11})_2$	1	0.480	−2.64	−0.048	0.537	2.62	0.045	0.057	0.509	−0.99
	2	0.291	−2.60	−0.048	0.353	2.60	0.046	0.062	0.322	−1.00
	3	−0.059	−12.36	−0.046	0.097	12.07	0.146	0.156	0.019	−0.98
	4	−0.196	−11.87	−0.181	−0.011	10.51	0.041	0.185	−0.104	−0.89
$Dy(PMo_{11})_2$	1	0.490	−2.53	−0.052	0.542	2.18	0.045	0.052	0.516	−0.86
	2	0.305	−2.61	−0.048	0.358	2.28	0.044	0.053	0.332	−0.87
	3	−0.054	−12.54	−0.049	0.116	11.23	0.151	0.170	0.031	−0.90
	4	−0.182	−12.58	−0.170	−0.002	11.15	0.039	0.180	−0.092	−0.89

first two Mo redox based processes for $Ln(PMo_{11})_2$ gave values of 1.24 and 1.30 confirming that the two first Mo-based electrochemical processes correspond to one-electron transfer; similar behaviour was obtained for $Nd(SiMo_7W_4)_2$ in aqueous solution.[25] Taking in consideration that $n \propto i_p^{2/3}$ in ref. 37 and comparing the peak currents of the first cathodic peak ($n = 1$) to the third and fourth processes in all $Ln(PMo_{11})_2$, it is possible to estimate the number of electrons involved in these more negative reduction processes: the values obtained were $n = 2.4$. However, these processes show much higher ΔE_p values than the expected for two-electron reversible process (0.030 V) suggesting quasi-reversible electron transfer processes.

Fig. 2(B) shows representative plots of log i_{pc} *vs.* log v for $Sm(PMo_{11})_2$. In the experimental timescale employed (scan rates in the range 0.02–0.3 V s^{-1}), the first two redox process shows slopes in the range 0.73–0.83, E_{pc}, E_{pa} values did not change significantly with scan rate (less than 0.01 V), suggesting electrochemical processes with mixed regime between kinetically and semi-infinite diffusion control. In the case of the third and fourth, plots of log i_{pc} *vs.* log v show slopes approximately 0.5 indicating semi-infinite diffusion controls for these electrochemical processes.

The influence of the pH of the electrolyte solution on the cyclic voltammetric profiles was also investigated. In Fig. 3(A) and (B) it is depicted, respectively, the cyclic voltammograms of $Sm(PMo_{11})_2$ under different pH conditions and the corresponding plot E_p *vs.* pH. The results show that the first and second redox processes are not affected by pH variation, in contrast to the third and fourth redox processes, which show marked dependence of peak potential and peak current with pH: the increase of pH, from 2.5 to 4.0, shifts the peak potentials to more negative values, while the peak currents gradually decrease. The dependence of E_p *vs.* pH corresponds to straight lines that show slopes between 0.070– 0.088 V/pH unit, ($0.999 \geqslant r \geqslant 0.991$), which indicates that the redox mechanism at these electrochemical processes requires the involvement of protons. In the experimental conditions used and assuming a Nernstian behaviour, the third and fourth Mo-based reductions in $Sm(PMo_{11})_2$, $Eu(PMo_{11})_2$, $Gd(PMo_{11})_2$, $Tb(PMo_{11})_2$ and $Dy(PMo_{11})_2$ correspond a two-electron/three-proton processes. The pH dependence of these electrochemical processes is related to the high negative charge of the polyanion at these reduced states.

In the case of semi-infinite diffusion controlled electrochemical processes, the diffusion coefficients can be estimated by applying the Randles–Sevcik equation:[38,39]

$$i_{pa} = 2.69 \times 10^5 n^{3/2} A D_r^{1/2} R_\infty v^{1/2}$$

where n is the number of electrons involved in the process, A is the electrode surface area (cm^2), D_r the diffusion coefficient (cm^2 s^{-1}), R the concentration of a species (mol cm^{-3}), v is scan rate (V s^{-1}) and i_{pa} the intensity of anodic peak current (A). Electrode surface area ($A = 7.25 \times 10^{-2}$ cm^2) was determined by chronoamperometry with a 1×10^{-3} mol dm^{-3} $K_3[Fe(CN)_6]$ in 1 mol dm^{-3} KCl

Table 4 UV visible spectra data of $Ln(PMo_{11})_2$ in pH 3.0 H_2SO_4/Na_2SO_4 buffer solution and corresponding reduced electrolysed solutions (r $Ln((PMo_{11})_2$, Ln = Sm, Eu, Gd; Tb and Dy) after electrochemical reduction at 0.1 V

Anion	λ (nm)/ε (cm^{-1} mol^{-1} dm^3)		
$Sm(PMo_{11})_2$	215 (14×10^4)	265 (3.0×10^4)	
r $Sm(PMo_{11})_2$	866 (6.6×10^3)	692 (5.3×10^3)	525 (2.8×10^3)
$Eu(PMo_{11})_2$	215 (12.5×10^4)	265 (3.9×10^4)	
r $Eu(PMo_{11})_2$	866 (5.0×10^3)	688 (3.9×10^3)	525 (2.0×10^3)
$Gd(PMo_{11})_2$	215 (14×10^4)	265 (4.5×10^4)	
r $Gd(PMo_{11})_2$	856 (6.2×10^3)	692 (4.9×10^3)	525 (2.7×10^3)
$Tb(PMo_{11})_2$	215 (7.9×10^4)	265 (3.0×10^4)	
r $Tb(PMo_{11})_2$	866 (6.0×10^3)	672 (4.6×10^3)	525 (2.5×10^3)
$Dy(PMo_{11})_2$	215 (9.0×10^4)	265 (4.8×10^4)	
r $Dy(PMo_{11})_2$	866 (6.2×10^3)	689 (4.9×10^3)	525 (2.3×10^3)

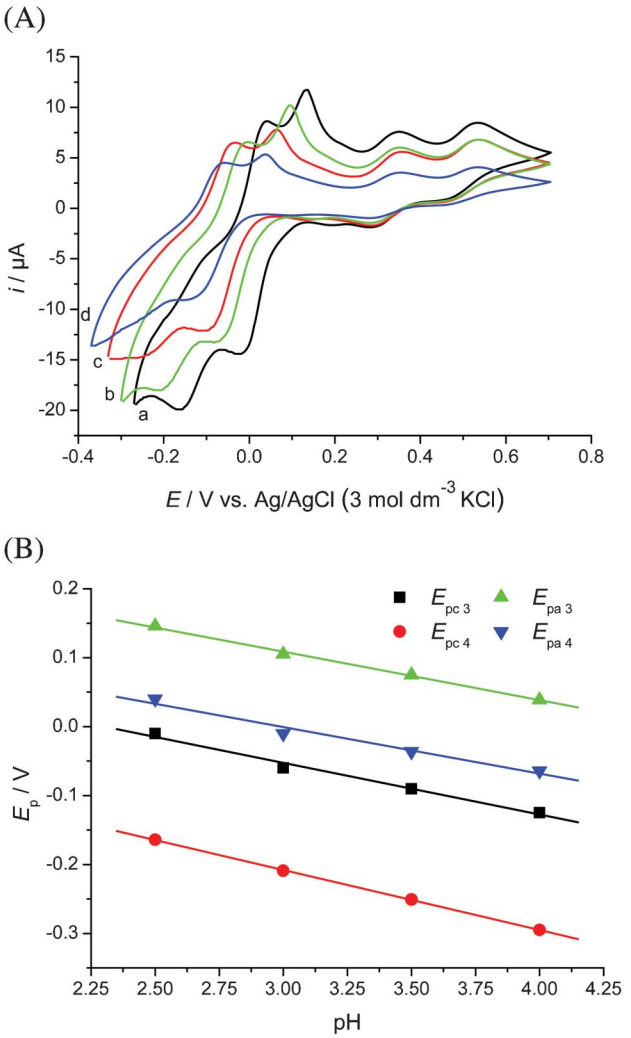

Fig. 3 A) Cyclic voltammograms of K^+ salts of $Sm(PMo_{11})_2$ (5×10^{-4} mol dm^{-3}) at $v = 0.05$ V s^{-1} for different pH values: (a) 2.5, (b) 3.0, (c) 3.5 and (d) 4.0. B) Plots of E_p *versus* pH of K^+ salt of $Sm(PMo_{11})_2$.

solution at 25 °C, where $D_r = 7.63 \times 10^{-6}$ cm^2 s^{-1}. The diffusion coefficients were estimated for the third process (E_{pc3}) where the reduction peak characteristics (ΔE_p and E_p $E_{p/2}$) were closer to what is expected for diffusion controlled reversible process: 3.2×10^{-6}, 2.3×10^{-6}, 3.1×10^{-6}, 2.2×10^{-6} and 3.2×10^{-6} cm^2 s^{-1} for $Sm(PMo_{11})_2$, $Eu(PMo_{11})_2$, $Gd(PMo_{11})_2$, $Tb(PMo_{11})_2$ and $Dy(PMo_{11})_2$, respectively in pH 3.0 H_2SO_4/Na_2SO_4 buffer solution. The effect of solution pH on the diffusion coefficients was also evaluated for $Sm(PMo_{11})_2$ and the values obtained were 3.3×10^{-6} (pH 2.5), 3.1×10^{-6} (pH 3.5) and 3.1×10^{-6} cm^2 s^{-1} (pH 4.0), what indicate that the pH of electrolyte solution does not affect significantly the diffusion coefficients of phosphomolybdates. No diffusion coefficients values were found in the literature concerning the sandwich type polyoxometalates $Ln(XM_{11})_2$ with X = P or Si, M = W or Mo. However, these values are of similar magnitude to polyoxometalates, for example $[SiW_{12}O_{40}]^{4-}$ that showed $D_r = 6.1 \times 10^{-6}$ cm^2 s^{-1} in aqueous solution (pH, 4.0).[40]

In order to evaluate the electrochromic properties of the $Ln(PMo_{11})_2$ solutions, electrolysis at two different potentials, 0.1 V (after the 2nd redox process) and 0.3 V (after the 4th redox process), were performed, and the electronic spectra of the reduced solutions were recorded in the range $200 < \lambda < 1100$ nm as a function of electrolysis time. During the electrolysis it was possible to observe a colour change of the solutions from yellow (oxidized state) to blue (reduced state) at the first electrolysis potential, and a darkening of the blue colour after the second electrolysis potential. The electronic spectra of all the reduced polyoxometalates are very similar and a representative example of the electroreduced solution spectra of $Tb(PMo_{11})$, at the two potentials, are depicted in Fig. 4 (A, C) as well as photographs of the corresponding electrolysed solutions; the electronic spectra of the electroreduced solutions (0.1 V) of the other POMs are presented in Fig. S4 in ESI.†

The electronic spectrum of the $Ln(PMo_{11})_2$ solution upon reduction at 0.1 V shows new four broad bands throughout the energy range studied, whose absorbance increases as a function of the electrolysis time: band A at $\lambda_{max} \approx 855$–$870$ nm, band B at $\lambda_{max} \approx 670$–$695$ nm, band C at $\lambda_{max} \approx 525$ nm and band D at $\lambda_{max} \approx 310$–$315$ nm. These bands show linear Abs. *vs.* electrolysis time dependencies up to approximately 400 min., as can be seen in Fig. 4(B) for the electroreduced $Tb(PMo_{11})$ species and similarly for the other four POMs studied (Fig. S4 in ESI†); the estimated molar absorption coefficients of all the electronic bands of all the reduced compounds are similar (in the range 2.0×10^3–6.6×10^3 cm^{-1} mol^{-1} dm^3), and are summarized in Table 4. Moreover, the ratios of the Abs increase *vs.* electrolysis time (slope values in Fig. 4(B)) for the electronic bands A, B and D are of the same magnitude, but band C shows a lower Abs increase ratio, what suggests that this bands is less dependent on the electrochemical reduction process. Although the electronic bands are very broad, no wavelength maxima shift is apparently observed.

Paralleling to the increase in Abs of the new electronic bands due to the new electroreduced species, there is also the expected decrease of the absorbance of the $O \rightarrow Mo^{VI}$ LMCT bands at $\lambda_{max} \approx 265$ and 215 nm of the oxidized $Ln(PMo_{11})$ species (not shown), since some of the Mo centres are being reduced.

The electrolysis at 0.3 V was only performed for fresh $Tb(PMo_{11})_2$ solutions since similar behaviour is expected for the other $Ln(PMo_{11})_2$ solutions. Fig. 4 (C) and (D) show, respectively, the electronic spectra for $Tb(PMo_{11})_2$ electroreduced solutions and the corresponding Abs *vs.* electrolysis time plot. Up to 10 min of electrolysis the four bands are also observed, but in this case, the intensity of bands A and B considerably increased and are slightly red-shifted, band C is only perceptible as a high energy shoulder on the intense band B, suggesting that its intensity does not change significantly with the reduction potentials; furthermore, after the initial 10 min of electrolysis, band D starts to decrease in intensity. The Abs *vs.* electrolysis time plots, Fig. 4(D), were obtained for bands A, B and D, and contrary to what was observed for the same study at 0.1 V, bands A and B have now a non-linear increase until they reach a plateau after approximately 90 min

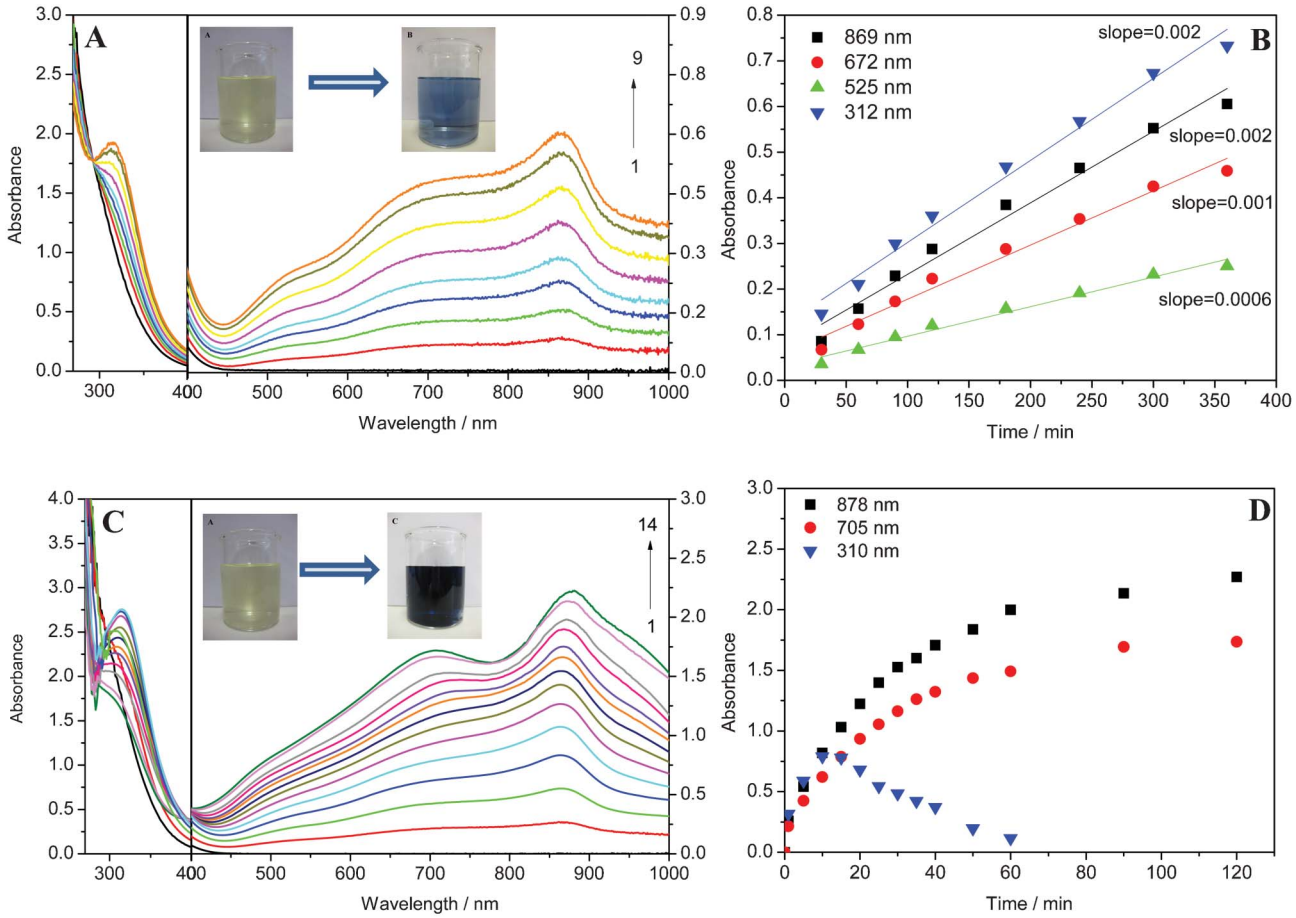

Fig. 4 UV visible spectra of$Tb(PMo_{11})_2$ salt in pH 3.0 H_2SO_4/Na_2SO_4 buffer after electrochemical reduction at: A) 0.1 V from 0 to 360 min (1 to 9), B) plot of Abs *vs.* electrolysis time, C) 0.3 V from 0 to 120 min (1 to 14) and D) plot of Abs *vs.* electrolysis time. The photographs of the solutions, before and after the electrolysis at 0.1 V and 0.3 V, are included in A and B plots, respectively.

of electrolysis. The ε values of bands A and B ($\varepsilon = 2.1 \times 10^4$ cm^{-1} mol^{-1} dm^3 and $\varepsilon = 1.6 \times 10^4$ cm^{-1} mol^{-1} dm^3, respectively) obtained for electroreduced at 0.3 V, corresponding to an addition of six electrons, are approximately three times the ε values obtained at 0.1 V (addition of two electrons).

As referred in literature the electronic spectra of photo- or electro-reduced polyoxometalates show intensity enhanced d–d bands in the visible region due to d^1 configuration of the reduced addenda atom (*ca.* W^V, Mo^V, V^{IV}) and intervalence charge transfer bands (IVCT), in the visible and near-IR regions, due to the presence of the mixed valence addenda atoms linked by oxygen atoms within the POM structure (*ca.* $W^V \rightarrow W^{VI}$, $Mo^V \rightarrow Mo^{VI}$, $V^{IV} \rightarrow V^V$).[7,36,41–44] As stated by Varga *et al.*[41] the molar absorption coefficients of the IVCT bands are roughly proportional to the number of electrons added and, consequently, the bands A and B of the electroreduced $Ln(PMo_{11})_2$ solutions can be assigned to $Mo^V \rightarrow Mo^{VI}$ IVCTs. Furthermore, band C, due to its low Abs dependence on the reduction potentials can be assign to a d–d transition from the d^1 Mo^V atoms. The assignment of band D is more intricate, since the majority of the electronic spectra of the photo or electro-reduced POM species described in literature usually report the data in the Vis-NIR region and not the near-UV region. Nevertheless, taking into account its Abs *vs.* electrolysis time behaviour for the two electrolysis, we can tentatively assign this band to an $O \rightarrow Mo^V$ charge transfer transition for the reduced $Ln(PMo_{11})_2$ species formed upon the two one-electron Mo-based reduction processes. Its disappearance during the electrolysis at more negative potentials is a consequence of the formation of more reduced POM species (corresponding to two-electron transfers) that will obviously have new charge transfer bands at different energies.

3.4. Photoluminescence

The photoluminescence characterization was performed for $Eu(PMo_{11})_2$ and $Tb(PMo_{11})_2$. Fig. 5 compares the excitation spectra of $Eu(PMo_{11})_2$ monitored within the more intense intra-$4f^6$ emission line (the $^5D_0 \rightarrow {}^7F_2$ transition) acquired at room temperature and at 12 K. The former spectra show a large band (full width at half maximum, fwhm, of *ca.* 80 nm) peaking at 258 nm which is ascribed to both $O \rightarrow Eu^{III}$ and $O \rightarrow Mo^{VI}$ LMCT transitions as already reported for other polyoxometalates containing Ln^{III} ions[45–47] and confirmed by their UV-Vis spectra (see above). This band is overlapped by a series of straight lines attributed to the $^7F_0 \rightarrow {}^5L_6$, $^5D_{2,1}$ and $^7F_1$

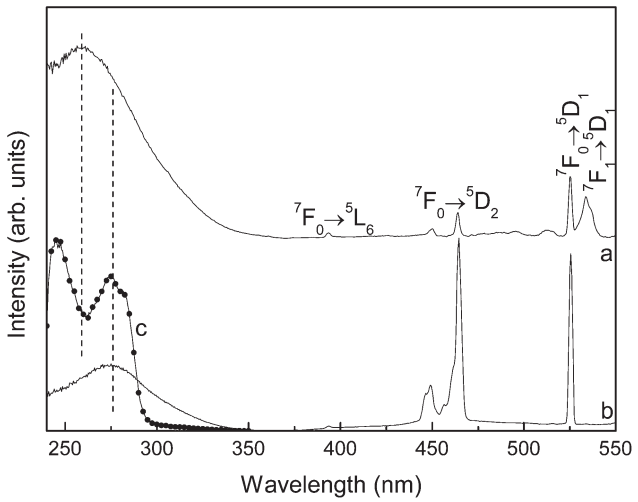

Fig. 5 Excitation spectra of $Eu(PMo_{11})_2$ acquired at (a) 300 K and (b) 12 K monitored at 614 nm. The excitation spectrum (curve c, full circles) was acquired at 12 K and monitored at 460 nm.

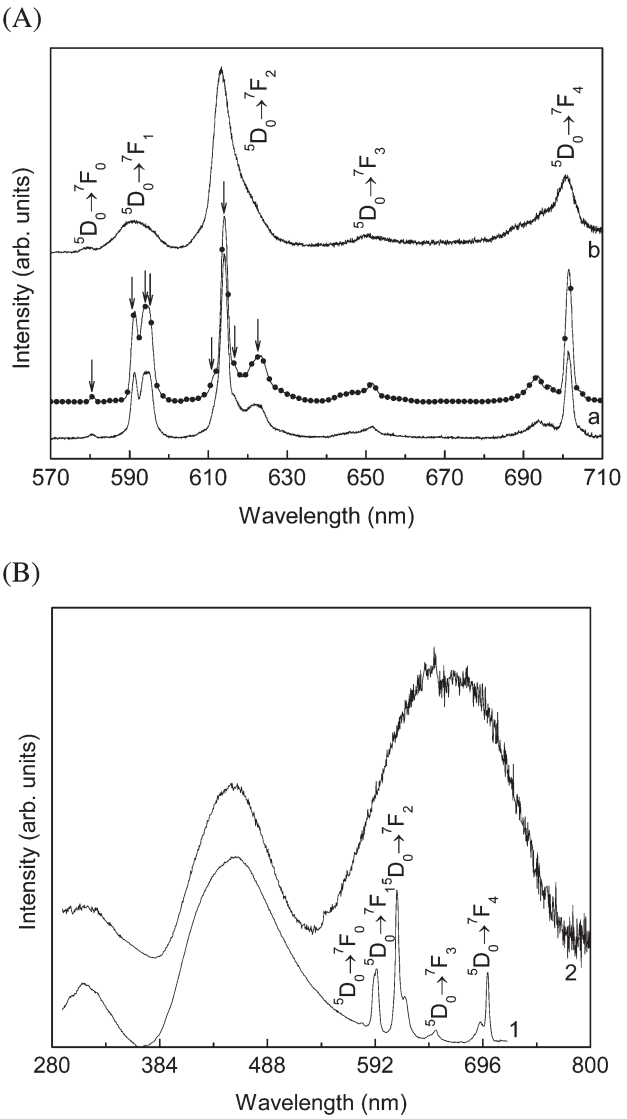

Fig. 6 A) High resolution emission spectra of the intra $4f^6$ lines for $Eu(PMo_{11})_2$ acquired at (a) 300 K and (b) 12 K excited at $\lambda = 270$ nm (solid lines) and 395 nm (full circles). B) Emission spectra for the (1) $Eu(PMo_{11})_2$ and (2) $Tb(PMo_{11})_2$ acquired at 12 K and exited at 270 nm.

$\rightarrow {}^5D_1$ transitions from Eu^{III}. The excitation spectrum acquired at 12 K is similar to that measured at 300 K, but it is observed a red-shift of the band to *ca.* 278 nm and an increase in the relative intensity of the intra-$4f^6$ transitions. The low-relative intensity of the broad band points out that, at 12 K, the Eu^{3+} excited states are mainly populated *via* direct intra-$4f^6$ excitation, rather than by the LMCT states, contrarily to that found at 300 K.

Under UV/Vis excitation, the emission spectra of the $Eu(PMo_{11})_2$ are formed of the typical Eu^{3+} emission in the visible spectral range (Fig. 6(A)) ascribed to the $^5D_0 \rightarrow {}^7F_{0-4}$ transitions. At 12 K, the emission spectra excited between 240 and 300 nm also reveal a large broad emission band between 280 and 600 nm, peaking at 310 and 460 nm (Fig. 5(B)), which are tentatively assigned to d–d bands identified in the absorption spectra (Fig. 4(A) and (C)).

For $Tb(PMo_{11})_2$ no sign of the intra-$4f^8$ Tb^{3+} transitions could be detected both at 12 and 300 K being observed the large broad emission bands already detected for the $Eu(PMo_{11})_2$ under excitation within 240–300 nm (Fig. 6(B)). The excitation paths for the broad band emission were selectively study for the $Eu(PMo_{11})_2$ compound by monitoring the excitation spectrum within 460 nm (Fig. 5). The spectrum reveals two components in the UV spectral region at 245 and 278 nm, overlapping the O $\rightarrow$ Eu and O $\rightarrow$ Mo LMCT states.

Focusing our attention on the Eu^{3+} emission, it is observed that the energy, number of Stark components and fwhm of the intra-$4f^6$ transitions are independent of the excitation wavelength, in good agreement with the presence of a single average local environment for the lanthanide ions, as X-ray diffraction results point out. Among the above mentioned three local point groups (D_{4h}, D_{2h} and C_{2v}) for the local symmetry of the Eu^{3+} ions, the first two groups have an inversion centre that is incompatible with the observed high relative intensity of the electric-dipole induced $^5D_0 \rightarrow {}^7F_2$ transition relatively to the magnetic-dipole $^5D_0 \rightarrow {}^7F_1$ one (Fig. 6(A)). Moreover, the presence of a single low-intensity line for the non-degenerated $^5D_0 \rightarrow {}^7F_0$ transition and the Stark splitting into 3 and 4 components for the $^5D_0 \rightarrow {}^7F_{1,2}$ transitions, respectively (marked with arrows in Fig. 6(A)) are in good agreement with a C_{2v} point symmetry group.[48,49] These results clearly point out differences in the Eu^{3+} local geometry when compared with the Gd^{3+}coordination centre, revealed in the respective crystal structure. While the EuO_8 coordination center approximate of a bicapped trigonal prismatic geometry, the environment of the GdO_8 centre resembles more a square-antiprism.

The $^5D_0$ emission-decay curves were monitored within the $^5D_0 \rightarrow {}^7F_2$ transition under intra-$4f^6$ excitation ($^5D_2$, 465 nm) at 12 and 300 K (Fig. S5 in ESI†). All the curves display a mono-exponential behavior, in accordance with a single average Eu^{3+} local environment. The single–exponential fit to the emission

decay curves yielded to $^5D_0$ lifetime values of 0.281 ± 0.010 ms and 1.671 ± 0.014 ms at 300 and 12 K, respectively. The significant increase observed in the lifetime value with the decreasing temperature, suggests the presence of thermally activated non-radiative mechanisms.

4. Conclusions

Five different sandwich-type lanthano-phosphomolybdates ($Ln^{III}(PMo_{11})_2$, where Ln^{III} = Sm, Eu, Gd, Tb and Dy) were successfully prepared and characterized. A pronounced similarity between the five compounds was found by the different techniques used for their characterization, mainly FT-IR, thermogravimetry, UV-Vis. spectroscopy and XRD powder diffraction. Furthermore, their electrochemical studies in aqueous solution showed that all present four Mo-based electrochemical reduction processes. The first two reduction processes present are unaffected by pH value and correspond to one-electron transfer. On the other hand, the more negative reduction processes are pH dependent and correspond to 2e / $3H^+$ processes.

Electrochromic studies showed that upon continuous electrolysis at two different potentials (0.1 and 0.3 V) the POMs undergo colour change from yellow to deep blue and new four electronic bands appear in the UV-Vis-NIR region. These electronic bands were assigned as follows based on their molar absorption coefficients (ε) and Abs variation as a function of electrolysis time: $Mo^V \rightarrow Mo^{VI}$ intervalence charge transfer transitions to the two bands in the range 855–670 nm, d–d transition due to d^1 configuration of the reduced Mo^V addenda atom to the band at $\lambda_{max} \approx 525$ nm, and finally the band at $\lambda_{max} \approx$ 310–315 nm, which was assigned to an $O \rightarrow Mo^V$ charge transfer transition.

Photo-luminescent studies were performed for $Eu(PMo_{11})_2$ and $Tb(PMo_{11})_2$. Both emission spectra display emission in the visible spectral region (tentatively ascribed to d–d transition transitions) that, in the case of the $Eu(PMo_{11})_2$, are overlapped by a series of intra-$4f^6$ lines, whose main excitation path is mediated by $O \rightarrow Eu^{III}$ and $O \rightarrow Mo^{VI}$ LMCT transitions.

These results provide valuable information for future applications of these compounds in the fabrication of dual-functional nanostructured films with electrochromic and photoluminescence properties.

Acknowledgements

The authors thank Fundação para a Ciência e a Tecnologia (FCT) and COMPETE for financial support through grants no. PEst-C/EQB/LA0006/2011 and PEst-C/CTM/LA0011/2011 and for specific funding toward the purchase of the single-crystal X-ray diffractometer. Authors also thank LSRE/LCM for the use of the thermogravimetric equipment. DMF also thanks FCT for her grant SFRH/BPD/74872/2010.

References

1 J. M. Clemente-Juan and E. Coronado, *Coord. Chem. Rev.*, 1999, **193–5**, 361–394.
2 P. Gomez-Romero, *Adv. Mater.*, 2001, **13**, 163–174.
3 D. E. Katsoulis, *Chem. Rev.*, 1998, **98**, 359–387.
4 J. T. Rhule, C. L. Hill and D. A. Judd, *Chem. Rev.*, 1998, **98**, 327–357.
5 A. Dolbecq, E. Dumas, C. R. Mayer and P. Mialane, *Chem. Rev.*, 2010, **110**, 6009–6048.
6 S. Q. Liu and Z. Y. Tang, *Nano Today*, 2010, **5**, 267–281.
7 T. Yamase, *Chem. Rev.*, 1998, **98**, 307–325.
8 P. M. S. Monk, R. J. Mortimer and D. R. Rosseinsky, *Electrochromism and Electrochromic Devices*, Cambridge Univ. Press, Cambridge, UK, 2007.
9 R. J. Mortimer, *Annual Reviews*, 2011, **41**, 241–268.
10 P. T. Hammond, *Adv. Mater.*, 2004, **16**, 1271–1293.
11 D. M. DeLongchamp and P. T. Hammond, *Adv. Funct. Mater.*, 2004, **14**, 224–232.
12 A. A. Argun, P. H. Aubert, B. C. Thompson, I. Schwendeman, C. L. Gaupp, J. Hwang, N. J. Pinto, D. B. Tanner and A. G. MacDiarmid Reynolds Jr, *Chem. Mater.*, 2004, **16**, 4401–4412.
13 M. Sadakane, A. Ostuni and M. T. Pope, *J. Chem. Soc., Dalton Trans.*, 2002, 63–67.
14 M. Sadakane, M. H. Dickman and M. T. Pope, *Angew. Chem., Int. Ed.*, 2000, **39**, 2914–2916.
15 P. Mialane, L. Lisnard, A. Mallard, J. Marrot, E. Antic-Fidancev, P. Aschehoug, D. Vivien and F. Secheresse, *Inorg. Chem.*, 2003, **42**, 2102–2108.
16 R. D. Peacock and T. J. R. Weakley, *J. Chem. Soc. A*, 1971, 1836–1839.
17 M. T. Pope, *Spring Verlag*, 1983.
18 L. C. W. Baker and D. C. Glick, *Chem. Rev.*, 1998, **98**, 3–49.
19 M. A. Fedotov, B. Z. Pertsikov and D. K. Danovich, *Polyhedron*, 1990, **9**, 1249–1256.
20 Y. K. Shan, Z. X. Liu, Z. S. Jin and G. C. Wei, *Acta Chim. Sin.*, 1992, **50**, 357–364.
21 E. B. Wang, Y. K. Shan, Z. X. Liu, J. F. Liu and B. J. Zhang, *Acta Chim. Sin.*, 1991, **49**, 774–781.
22 A. J. Gaunt, I. May, M. J. Sarsfield, D. Collison, M. Helliwell and I. S. Denniss, *Dalton Trans.*, 2003, 2767–2771.
23 R. Copping, A. J. Gaunt, I. May, M. J. Sarsfield, D. Collison, M. Helliwell, I. S. Denniss and D. C. Apperley, *Dalton Trans.*, 2005, 1256–1262.
24 M. J. Liu and S. J. Dong, *Electrochim. Acta*, 1995, **40**, 197–200.
25 L. Cheng, X. M. Zhang, X. D. Xi, B. F. Liu and S. J. Dong, *J. Electroanal. Chem.*, 1996, **407**, 97–103.
26 L. Pettersson, I. Andersson and L. O. Ohman, *Inorg. Chem.*, 1986, **25**, 4726–4733.
27 L. A. Combswalker and C. L. Hill, *Inorg. Chem.*, 1991, **30**, 4016–4026.
28 T. Kottke and D. Stalke, *J. Appl. Crystallogr.*, 1993, **26**, 615–619.
29 APEX2, *Data Collection Software* Version 2.1-RC13, Bruker AXS, Delft, The Netherlands, 2006.
30 Cryopad, *Remote monitoring and control*, Version 1.451, Oxford Cryosystems, Oxford, United Kingdom, 2006.
31 SAINT+, *Data Integration Engine* v. 7.23a ©, 1997–2005, Bruker AXS, Madison, Wisconsin, USA.

32 G. M. Sheldrick, SADABS v.2.01, *Bruker/Siemens Area Detector Absorption Correction Program*, 1998, Bruker AXS, Madison, Wisconsin, USA..
33 G. M. Sheldrick, *Acta Crystallogr., Sect. A: Found. Crystallogr.*, 2008, **64**, 112–122.
34 G. M. Sheldrick, SHELXS-97, *Program for Crystal Structure Solution*, University of Göttingen, 1997.
35 G. M. Sheldrick, SHELXL-97, *Program for Crystal Structure Refinement*, University of Göttingen, 1997.
36 H. So and M. T. Pope, *Inorg. Chem.*, 1972, **11**, 1441–1443.
37 A. J. Bard and L. R. Faulkner, *Electrochemical Methods*, Wiley, New York, 2001.
38 A. M. O. Brett and C. M. A. Brett, *Electroquímica: Princípios, Métodos e Aplicações*, Oxford University Press, 1993.
39 C. M. A. Brett and A. M. O. Brett, *Electroanalysis*, Oxford Chemistry Primers, 1998.
40 L. C. W. Baker and M. T. Pope, *J. Am. Chem. Soc.*, 1960, **82**, 4176–4179.
41 G. M. Varga Papaconstantinou and M. T. Pope, *Inorg. Chem.*, 1970, **9**, 662–667.
42 R. A. Prados and M. T. Pope, *Inorg. Chem.*, 1976, **15**, 2547–2553.
43 A. M. Douvas, K. Yannakopoulou and P. Argitis, *Chem. Mater.*, 2010, **22**, 2730–2740.
44 T. Akutagawa, F. Kudo, R. Tsunashima, S. Noro, L. Cronin and T. Nakamura, *Inorg. Chem.*, 2011, **50**, 6711–6718.
45 R. Ballardini, Q. G. Mulazzani, M. Venturi, F. Bolletta and V. Balzani, *Inorg. Chem.*, 1984, **23**, 300–305.
46 M. Sugeta and T. Yamase, *Bull. Chem. Soc. Jpn.*, 1993, **66**, 444–449.
47 F. L. Sousa, M. Pillinger, R. A. S. Ferreira, C. M. Granadeiro, A. M. V. Cavaleiro, J. Rocha, L. D. Carlos, T. Trindade and H. I. S. Nogueira, *Eur. J. Inorg. Chem.*, 2006, 726–734.
48 Q. Ju, Y. S. Liu, R. F. Li, L. Q. Liu, W. Q. Luo and X. Y. Chen, *J. Phys. Chem. C*, 2009, **113**, 2309–2315.
49 K. Binnemans and C. GorllerWalrand, *J. Rare Earths*, 1996, **14**, 173–180.